Supporting information

Room Temperature Spin Hall Effect in Graphene/MoS_2 van der Waals Heterostructures

C. K. Safeer[1,‡], Josep Ingla-Aynés[1,‡], Franz Herling[1,‡], José H. Garcia[2], Marc Vila[2,3], Nerea Ontoso[1], M. Reyes Calvo[1,4], Stephan Roche[2,5], Luis E. Hueso[1,4], Fèlix Casanova[1,4,*].

[1] CIC nanoGUNE, 20018 Donostia-San Sebastian, Basque Country, Spain.
[2] Catalan Institute of Nanoscience and Nanotechnology (ICN2), CSIC and The Barcelona Institute of Science and Technology, Campus UAB, 08193 Bellaterra, Catalonia, Spain.
[3] Department of Physics, UniversitatAutònoma de Barcelona, Campus UAB, 08193 Bellaterra, Catalonia, Spain.
[4] IKERBASQUE, Basque Foundation for Science, 48013 Bilbao, Basque Country, Spain.
[5] ICREA – Institució Catalana de Recerca i Estudis Avançats, 08010 Barcelona, Catalonia, Spain.

[‡]These authors contributed equally to this work
*E-mail: f.casanova@nanogune.eu

Table of contents:

S1. Analysis of the conventional (symmetric) Hanle precession measurements

S1.1. Standard model

To extract the spin transport parameters of the pristine graphene channel and determine the spin injection efficiency of the ferromagnetic (FM) electrodes, we have performed conventional symmetric Hanle precession experiments in the pristine graphene region. These are performed by measuring the nonlocal resistance of the reference graphene lateral spin valve (LSV) while having a parallel (R_P) or antiparallel (R_{AP}) orientation of the FM electrode magnetizations and applying a magnetic field in the x direction (B_x) (i.e., perpendicular to the easy axis of the FM), as shown in Figure S1a for the case of Sample A at 10 K. Finally, the spin transport parameters have been obtained from fitting to the following equation[1]:

$$\Delta R_{NL} = R_P - R_{AP} = \frac{P_{sym}^2 \cos^2(\beta) R_{sq}^{gr} \lambda_s^{gr}}{W_{gr}} Re\left\{ \frac{e^{-\frac{L}{\lambda_s^{gr}}\sqrt{1-i(\omega-\omega_0)\tau_s^{gr}}}}{\sqrt{1-i(\omega-\omega_0)\tau_s^{gr}}} \right\} + R_0 \qquad \text{(S1)}$$

Here, $P_{sym}^2 = P_i P_d$ is the product of the injector and detector spin polarization respectively, β is the angle between the contact magnetization and the easy axis [see Figure S1b], R_{sq}^{gr} is the square resistance of the graphene channel, $\lambda_s^{gr} = \sqrt{D_s^{gr}\tau_s^{gr}}$ is the spin relaxation length, D_s^{gr} is the spin diffusion coefficient, τ_s^{gr} is the spin lifetime, W_{gr} is the channel width, $\omega = g\mu_B B_x/\hbar$ is the Larmor frequency, $g = 2$ is the Landé factor, μ_B is the Bohr magneton, and $\hbar$ is the reduced Plank constant. Finally, $\omega_0 = g\mu_B B_0/\hbar$ accounts for a small remanescensefrom the magnet and R_0 is the background signal. Equation S1 assumes that spin transport is 1D and the contact resistances are much higher than the channel spin resistance [2] ($R_N^{gr} = R_{sq}^{gr}\lambda_s^{gr}/W_{gr}$).

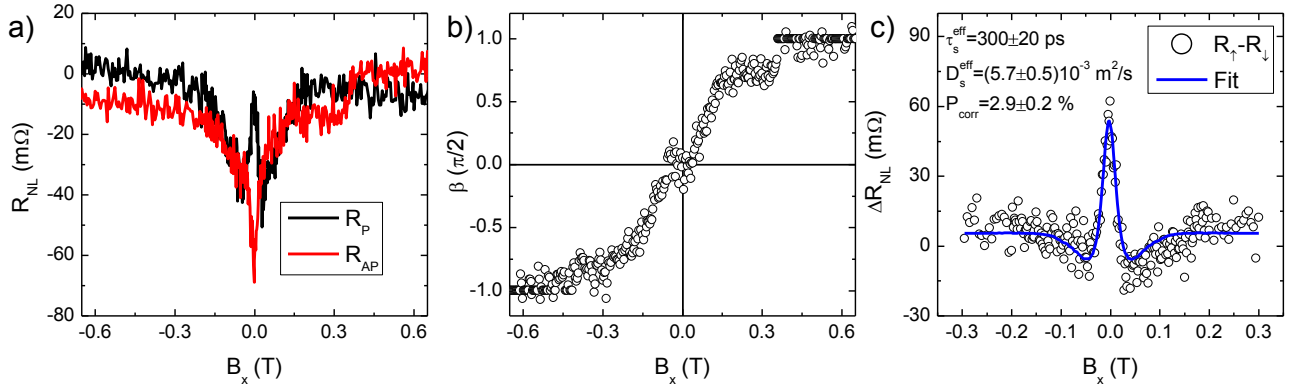

Figure S1. (a) Conventional Hanle precession data in the parallel and antiparallel contact magnetization configurations for sample A at 10 K. (b) Angle between the contact magnetization and the easy axis extracted from the Hanle data in a) as described in the text below. (c) Spin signal calculated using $R_P - R_{AP}$ from the Hanle data in (a) with the corresponding fit using Eq. S1 and extracted parameters. $P_{corr}$is the spin polarization obtained using the model with an extra arm described in Section S2 and the fit parameters as inputs.

Since B_x is applied perpendicular to the easy axis of a FM, it pulls its magnetization by an angle β in the field direction[3]. To determine β, we use the fact that the measured nonlocal resistance [FigureS1a] does not include only the precessing component described above, but also includes a signal which is generated by the spins which are injected parallel to the $B_x$direction as the contact magnetizations are pulled. This term is proportional to $\sin^2(\beta)$ and appears in both R_P and R_{AP} with

the same sign. Because the precessing component has opposite sign for R_P and R_{AP}, $R_P + R_{AP}$ is proportional to $\sin^2(\beta)$. To obtain the data plotted in Figure S1b, we have normalized $0 < R_P + R_{AP} < 1$, and taken the arcsine of its square root to obtain β as a function of the magnetic field. Finally, to guarantee that the extracted β at $B_x = 0$ is zero and that it reaches $\pi/2$ at high B, we have renormalized the result of this operation. At $B = 0.4$ T, we see a jump in β, which we attribute to a switch of one of the magnetizations. To prevent this step from affecting our analysis, we have used only the negative B result for the fits, such as the one shown in Figure S1c where the spin signal $R_P - R_{AP}$ is fit to Eq. S1. The obtained fit parameters are shown in the blue rows of Table S1 (sample A) and Table S2 (sample B).

In the case of sample A, the reference graphene LSV has two extra arms (the Hall bar) connected to the main channel, which implies that spins are also diffusing towards these arms. To account for the effect of the arms on the spin polarization we have assumed that spin propagation is 1D and the arms are much longer than the spin relaxation length. As a consequence, the shape of the Hanle curve (determined by D_s^{Gr} and τ_s^{Gr}) is not affected within our model by the presence of the extra arms and only the spin injection and detection efficiencies have to be adjusted. The spin transport parameters extracted from the fit are used as inputs to the three-arm model described in Section S1.2 to determine a better estimate of the contact spin polarization, which we call P_{corr}.

For Sample B, the symmetric Hanle curves were taken in a reference LSV without any cross between spin injector and detector, hence, P_i is extracted directly from the fit of $\Delta R_{NL} = R_P - R_{AP}$ to Eq. S1.

S1.2. Three-arm model

The original geometry we want to model for the reference graphene LSV used in Sample A is shown in Figure S2a.

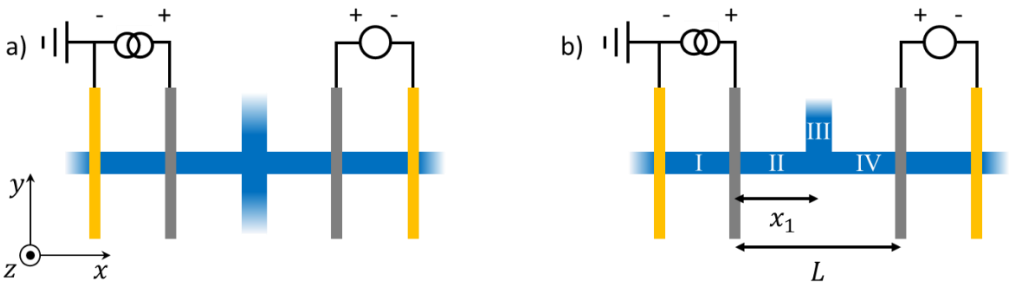

Figure S2. (a) 1D approximation of the reference device geometry for Sample A. (b) Simulated device geometry. The width of the top arm is two times the width of the arms in the device and in (a) and the white numbers correspond to the different modelling regions (see discussion below).

However, because we are interested in the spins that diffuse towards the middle arm and the spin transport is fully diffusive, the two arms can be simplified down to one with twice the width [see Figure S2b]. The most important assumptions here are 1D spin transport and non-invasive contacts. The left contact is the injector and the right one the detector.

To calculate the spin signal, one needs to define the spin accumulation, which is a solution of the Bloch equations considering a magnetic field applied in the z direction[4]:

$$D_s^{gr}\frac{d^2\mu_x}{dx^2} - \frac{\mu_x}{\tau_s^{gr}} - \omega\mu_y = 0$$

$$D_s^{gr}\frac{d^2\mu_y}{dx^2}-\frac{\mu_y}{\tau_s^{gr}}+\omega\mu_x=0$$

Note that here we have considered that the magnetic field is applied in the z direction for analogy with the conventional Hanle precession, but we are applying a magnetic field along x. We have done this because the solution for μ_y is the same in both cases for an isotropic system such as pristine graphene. The general solution for μ_y for each region can be written as:

$$\mu_I^y = Ae^{\frac{x}{\lambda_s^{gr}}\sqrt{1+i\omega\tau_s^{gr}}}+Be^{\frac{x}{\lambda_s^{gr}}\sqrt{1-i\omega\tau_s^{gr}}}$$
$$\mu_{II}^y = Ce^{\frac{x}{\lambda_s^{gr}}\sqrt{1+i\omega\tau_s^{gr}}}+De^{\frac{x}{\lambda_s^{gr}}\sqrt{1-i\omega\tau_s^{gr}}}+Ee^{-\frac{x}{\lambda_s^{gr}}\sqrt{1+i\omega\tau_s^{gr}}}+Fe^{-\frac{x}{\lambda_s^{gr}}\sqrt{1-i\omega\tau_s^{gr}}}$$
$$\mu_{III}^y = Ge^{-\frac{x}{\lambda_s^{gr}}\sqrt{1+i\omega\tau_s^{gr}}}+He^{-\frac{x}{\lambda_s^{gr}}\sqrt{1-i\omega\tau_s^{gr}}}$$
$$\mu_{IV}^y = Ie^{-\frac{x}{\lambda_s^{gr}}\sqrt{1+i\omega\tau_s^{gr}}}+Je^{-\frac{x}{\lambda_s^{gr}}\sqrt{1-i\omega\tau_s^{gr}}}$$

From the Bloch equations we obtain an expression for μ_x:

$$\mu_x=-\frac{D_s^{gr}}{\omega}\frac{d^2\mu_y}{dx^2}+\frac{\mu_y}{\omega\tau_s^{gr}}$$

which results, at the different regions,

$$\mu_I^x = -iAe^{\frac{x}{\lambda_s^{gr}}\sqrt{1+i\omega\tau_s^{gr}}}+iBe^{\frac{x}{\lambda_s^{gr}}\sqrt{1-i\omega\tau_s^{gr}}}$$
$$\mu_{II}^x = -iCe^{\frac{x}{\lambda_s^{gr}}\sqrt{1+i\omega\tau_s^{gr}}}+iDe^{\frac{x}{\lambda_s^{gr}}\sqrt{1-i\omega\tau_s^{gr}}}-iEe^{-\frac{x}{\lambda_s^{gr}}\sqrt{1+i\omega\tau_s^{gr}}}+iFe^{-\frac{x}{\lambda_s^{gr}}\sqrt{1-i\omega\tau_s^{gr}}}$$
$$\mu_{III}^x = -iGe^{-\frac{x}{\lambda_s^{gr}}\sqrt{1+i\omega\tau_s^{gr}}}+iHe^{-\frac{x}{\lambda_s^{gr}}\sqrt{1-i\omega\tau_s^{gr}}}$$
$$\mu_{IV}^x = -iIe^{-\frac{x}{\lambda_s^{gr}}\sqrt{1+i\omega\tau_s^{gr}}}+iJe^{-\frac{x}{\lambda_s^{gr}}\sqrt{1-i\omega\tau_s^{gr}}}$$

To determine the spin accumulation in the system we need to determine the coefficients $A-H$. This is done by applying the following boundary conditions. First, we impose the continuity of μ^x and μ^yat $x=0$ (intersection point between regions I and II) and $x=x_1$ (intersection point between regions II, III, and IV). From these conditions, we obtain 6 equations. Second, we define the spin current as $I_s^i=-\frac{W_{gr}}{eR_{sq}^{gr}}\frac{d\mu_s^i}{dx}$ where i refers to the spin polarization direction of the spin accumulation (x or y). Next, we impose the continuity of I_s^x and I_s^y at $x=x_1$ and the continuity of $I_s^x$and discontinuity of I_s^y of P_iI_c, where $P_i$is the injector polarization and I_c the applied current, at $x=0$. This gives the 4 equations that we are missing.

Finally, the solution for the spin signal is:

$$\Delta R_{NL}=R_P-R_{AP}=\frac{2P_d\mu_{IV}^y(L)}{eI_c}=\frac{2P_d}{eI_c}\left(Ie^{-\frac{L}{\lambda_s^{gr}}\sqrt{1+i\omega\tau_s^{gr}}}+Je^{-\frac{L}{\lambda_s^{gr}}\sqrt{1-i\omega\tau_s^{gr}}}\right)$$

In the final solution, both I and J are proportional to P_i and, hence, the spin signal is proportional to $P_i P_d = P_{corr}^2$.

Here, we use the above equation together with the spin transport parameters in the pristine graphene region obtained from the fit to Eq. S1 and the magnitude of the measured spin signal to obtain P_{corr}, that is the average spin polarization of the ferromagnetic contacts.

S2. Analysis of the (antisymmetric) Hanle precession measurements with spin Hall detection

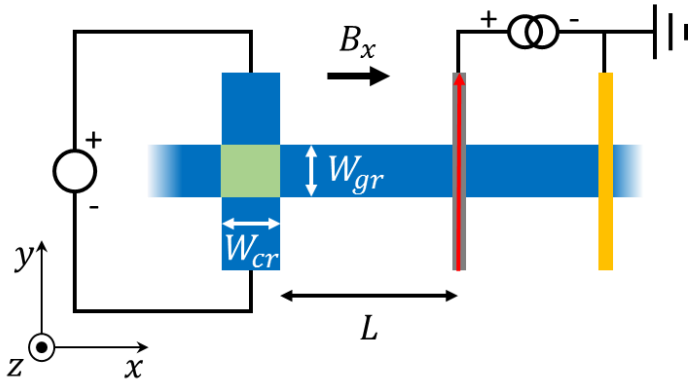

Figure S3. Sketch of the measured geometry with the positive magnetic field and the "up" direction of the magnetization indicated with arrows. The green area is covered by a TMD and is where the spin-to-charge conversion takes place.

When a spin current density I_s/W_{gr} enters a region with high spin-orbit coupling, it generates a transverse charge current density $I_c^T/W_{cr} = \theta_{SH}^{TMD/gr} I_s/W_{gr}$ via the inverse spin Hall effect, here θ_{SH} is the spin Hall angle and W_{cr} the length of the high spin-orbit coupling region (see Figure S3). This generates a transverse voltage V_{SH}

$$\frac{V_{SH}}{W_{cr}R_{gr}} = \frac{I_c^T}{W_{cr}} = \frac{\theta_{SH}^{TMD/gr} I_s}{W_{gr}} \rightarrow V_{SH} = \frac{\theta_{SH}^{TMD/gr} R_{gr} W_{cr} I_s}{W_{gr}}$$

where $R_{gr} = R_{sq}^{TMD/gr} W_{gr}/W_{cr}$ is the resistance for the transverse current that determines the conversion from an induced current to a voltage. Note that $R_{sq}^{TMD/gr}$ is the square resistance of the TMD-covered graphene region. Therefore,

$$V_{SH} = \frac{\theta_{SH}^{Gr} R_{sq}^{TMD/gr} W_{gr} W_{cr} I_s}{W_{cr} W_{gr}} = \theta_{SH}^{Gr} R_{sq}^{TMD/gr} I_s$$

To obtain the spin currents propagating in our device, we assume that it is homogeneous and isotropic, and the propagation is 1D. Because the transport properties of the TMD-covered region are not the same as those of the pristine graphene region, we will extract effective parameters (τ_s^{eff}, D_s^{eff}, and λ_s^{eff}) from the homogeneous fit. These parameters are an average for both the pristine and the TMD-covered graphene regions.

The out-of-plane (z direction) spin accumulation (μ_z) at a distance L from the spin injector, which induced by spin precession around a magnetic field applied in the x direction is written as [4,5].

$$\mu_z = \pm \frac{P_i e I_c R_{sq}^{gr} \lambda_s^{eff}}{2W_{gr}} Im \left\{ \frac{e^{-\frac{L}{\lambda_s^{eff}}\sqrt{1-i\omega\tau_s^{eff}}}}{\sqrt{1-i\omega\tau_s^{eff}}} \right\}$$

Here, P_i the spin injection efficiency of the injector, I_c the bias current. The $\pm$ corresponds to the up and down direction of the injector magnetization defined as in Figure S3.

The spin current is defined as:

$$I_s = I_\uparrow - I_\downarrow = \frac{W_{gr}}{eR_{sq}^{Gr}} \frac{d\mu_z}{dx} = \pm \frac{P_i I_c}{2} Im \left\{ e^{-\frac{L}{\lambda_s^{eff}}\sqrt{1-i\omega\tau_s^{eff}}} \right\}$$

Then the signal induced by this spin current is:

$$R_{SH} = \frac{V_{SH}}{I_c} = \frac{\theta_{SH}^{Gr} R_{sq}^{TMD/gr} I_s}{I_c} = \pm \frac{\theta_{SH}^{Gr} P_i R_{sq}^{TMD/gr}}{2} Im \left\{ e^{-\frac{L}{\lambda_s^{eff}}\sqrt{1-i\omega\tau_s^{eff}}} \right\}$$

However, in our geometry, we have a cross with a width W_{cr} (Figure S3) that is comparable to the spin relaxation length. Therefore, I_s needs to be replaced by the average spin current $\overline{I_s} = \frac{1}{W_{cr}} \int_L^{L+W_{cr}} I_s dx$. The result from this operation is:

$$R_{SH} = \frac{\theta_{SH}^{TMD/gr} R_{sq}^{TMD/gr} \overline{I_s}}{I_c} = \pm \frac{\theta_{SH}^{TMD/gr} P_i R_{sq}^{TMD/gr} \lambda_s^{eff}}{2W_{cr}} Im \left\{ \frac{e^{-\frac{L}{\lambda_s^{eff}}\sqrt{1-i\omega\tau_s^{eff}}}}{\sqrt{1-i\omega\tau_s^{eff}}} - \frac{e^{-\frac{L+W_{cr}}{\lambda_s^{eff}}\sqrt{1-i\omega\tau_s^{eff}}}}{\sqrt{1-i\omega\tau_s^{eff}}} \right\}$$

To remove any signal which does not come from the y-component of the injector magnetization in our measurement we subtract both injector configurations to

$$\Delta R_{SH} = R_{SH}^{\uparrow} - R_{SH}^{\downarrow} = \frac{P_{anti}^2 R_{sq}^{TMD/gr} \lambda_s^{eff}}{W_{cr}} Im \left\{ \frac{e^{-\frac{L}{\lambda_s^{eff}}\sqrt{1-i(\omega-\omega_0)\tau_s^{eff}}}}{\sqrt{1-i(\omega-\omega_0)\tau_s^{eff}}} - \frac{e^{-\frac{L+W_{cr}}{\lambda_s}\sqrt{1-i(\omega-\omega_0)\tau_s^{eff}}}}{\sqrt{1-i(\omega-\omega_0)\tau_s^{eff}}} \right\} + R_0 \text{(S2)}$$

where $R_{SH}^{\uparrow}$ and $R_{SH}^{\downarrow}$correspond to the spin Hall component of the nonlocal resistance of the graphene/TMD lateral device (Figure S3) while orienting the FM injector along the$+y$ and $-y$ direction, respectively, and applying B in the x direction, which leads to antisymmetric Hanle precession curves. The measured signal with these injector configurations is called $R_{nl}^{\uparrow}$ and $R_{nl}^{\downarrow}$. Note that we have also added the term $\cos(\beta)$ to account for the effect of the magnetic field on the magnetization direction of the FM injector. Equation S2 has been used to fit to the antisymmetric Hanle precession curves such as the ones shown in Figure S4. From the fit we obtain the effective

τ_s^{eff}, D_s^{eff} and P_{anti} of the channel, which are averaged over the pristine graphene and TMD-covered regions. Note that $P_{anti} = \sqrt{P_i \theta_{SH}^{TMD/gr}}$ depends on both the injector spin polarization P_i and the spin Hall angle $\theta_{SH}^{TMD/gr}$. To determine $\theta_{SH}^{TMD/gr}$ we assume that $P_i = P_{corr}$ for Sample A and $P_i = P_{sym}$ for sample B obtained from the symmetric Hanle curve (Section S1). The fitted parameters are shown in the orange rows of Table S1 (Sample A) and Table S2 (Sample B).

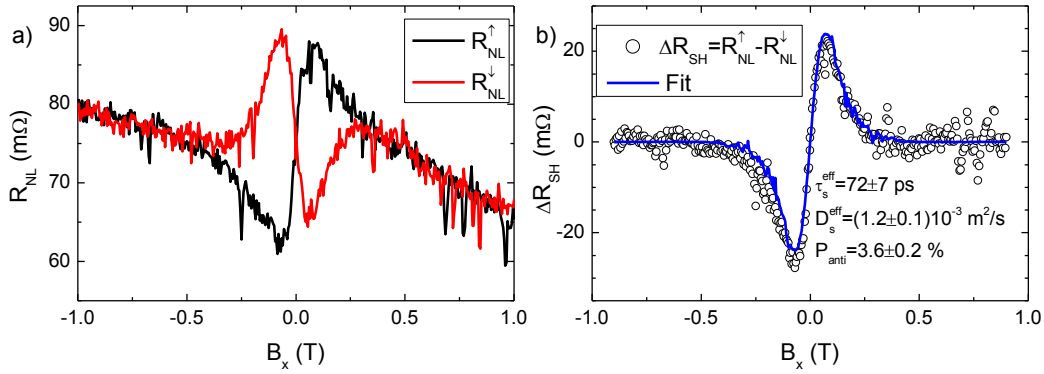

Figure S4. (a) Antisymmetric Hanle precession measurements for the two different orientations of the FM injector for Sample A at 10 K. Note that we have called $R_{NL}^{\uparrow}$ and $R_{NL}^{\downarrow}$ the signals measured with the magnetization of the spin injector aligned in the $+y$ and $-y$ direction respectively. (b) ΔR_{SH} and its fit to Eq. S2 with the extracted parameters.

S3. Measurement of spin Hall signals obtained with the spin injector placed at the right and left side of the Hall cross

Since the spin signal is induced by the spin current, which points in the graphene plane, it should change sign when the spin injector is changed from the right to the left side of the Hall cross. Note that, if the spin signal would be induced by spin absorption in the TMD, it would not change sign. This control experiment has been performed in sample B, where the two measurements shown in Figure S5 confirm that the signal is induced by the spin current propagating in the graphene plane.

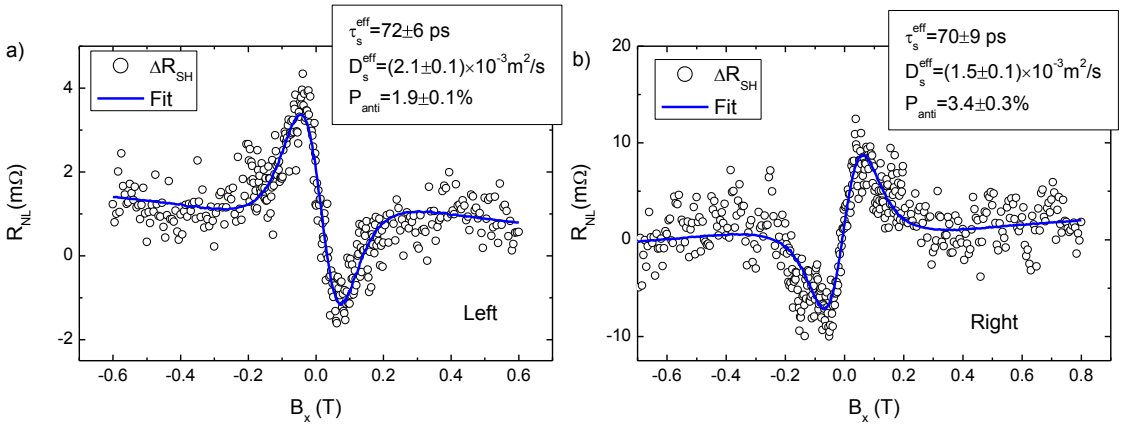

Figure S5. Antisymmetric Hanle curves obtained by subtracting the measurements obtained for both magnetic configurations of the FM injector at 10 K in sample B, for the (a) left and (b) right spin injectors.

We see that, as expected, the spin transport parameters (τ_{fit} and D_{fit}) extracted from both Hanle curves are very similar. However, because the magnitude of the spin signals is different, the spin polarizations extracted from both curves show a discrepancy of almost a factor of two. This is caused by the fact that, in both cases we are using different spin injectors which have different efficiencies.

In Table S2, this has consequences on the determination of $\theta_{SH}^{TMD/gr}$. To avoid this discrepancy, we rely on the measurements performed using the right injector, in which the spin injector is the same as for the reference Hanle curves.

S4. Analysis of the μ_x-induced spin-to-charge conversion signal

S4.1. Extraction of the signal

As explained above, when a magnetic field B_x is applied perpendicular to the easy axis of a FM electrode, its magnetization rotates an angle βin the direction of the field. In our geometry, this results in the injection of spins in the direction of the magnetic field independently of the initial magnetization direction and, therefore, this component can be extracted calculating $R_{SCC} = (R_{NL}^{\uparrow} + R_{NL}^{\downarrow})/2$. The result from this operation is shown in Figure S6 for the case of Sample A at 10 K.

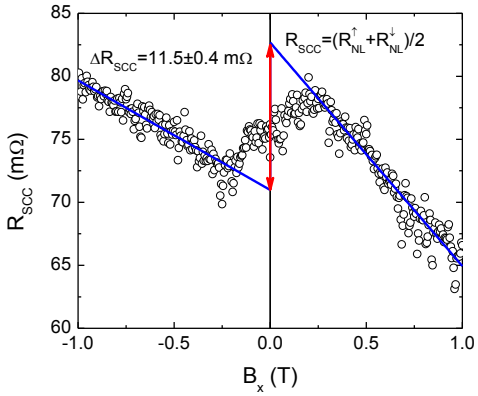

Figure S6. μ_x-induced spin-to-charge conversion signal R_{SCC} obtained by averaging the antisymmetric Hanle precession curves measured for both magnetic configurations of the FM injector at 10 K for Sample A [Figure S4a]. The magnitude of the spin-to-charge conversion signal (ΔR_{SCC}) is quantified by calculating the zero-field extrapolation using linear fittings to the spin signal at high positive and negative fields.

The S-shaped signal saturates at around $\pm$240 mT, which is the saturation field for the magnetization of the FM injector [see Figure S1b]. This result indicates that the source of this signal depends on the x component of the spin accumulation (μ_x). Because there is a background which has different slope for positive and negative magnetic fields, we extrapolate the high B data to $B_x = 0$ to extract the magnitude of this component. As discussed in the main manuscript, this means that it can be caused either by the Rashba-Edelstein effect in the graphene layer or the spin Hall effect in the MoS_2 semiconducting channel after spin absorption.

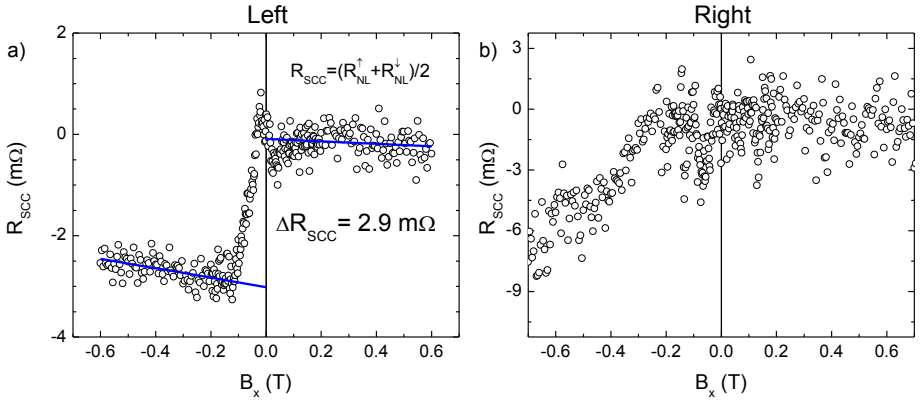

Figure S7. R_{SCC}signal at 10 K for Sample B measured with spins injected by a FM electrode placed on (a) the right and (b) the left side of the TMD-covered region.

We have performed the same operation on the measurements obtained from Sample B and the results at 10 K are plotted in Figure S7. In contrast with the left injector, the right one does not show any μ_x-induced spin-to-charge conversion feature.

S4.2. Quantification of the Rashba-Edelstein effect

For the Rashba-Edelstein case, a spin accumulation in the x direction (μ_x) induces a charge current density in the y direction $J_c^T = I_c^T/W_{cr}$ with an efficiency γ that is the conversion efficiency: $\mu_x\gamma = \frac{I_c^T}{W_{cr}} = \frac{V_{RE}}{W_{cr}R_{gr}}$. As a consequence, $V_{RE} = \overline{\mu_x}\gamma R_{sq}W_{gr}$ where $\bar{\mu}_x = \frac{1}{W_{cr}}\int_L^{L+W_{cr}} \mu_x(x)dx$ is the average spin accumulation at the cross, which is defined as $\mu_x = \pm\frac{eP_iIR_{sq}^{TMD/gr}\lambda_s^{eff}}{2W_{gr}} e^{-\frac{x}{\lambda_s^{eff}}}$ where + and – correspond to the positive and negative magnetization directions of the spin injector corresponding to positive and negative magnetic field respectively.

$$\begin{aligned}
\bar{\mu}_x &= \frac{1}{W_{cr}}\int_L^{L+W_{cr}} \mu_x(x)dx = \pm\frac{eP_iI_cR_{sq}^{TMD/gr}\lambda_s^{eff}}{2eW_{gr}}\frac{1}{W_{cr}}\int_L^{L+W_{cr}} e^{-x/\lambda_s^{eff}}dx \\
&= \pm\frac{eP_iI_cR_{sq}^{TMD/gr}\lambda_s^{eff}}{2W_{gr}}\frac{1}{W_{cr}}\left[-\lambda_s^{eff}e^{-\frac{x}{\lambda_s^{eff}}}\right]_L^{L+W_{cr}} \\
&= \pm\frac{eP_iI_cR_{sq}^{TMD/gr}{\lambda_s^{eff}}^2}{2W_{gr}W_{cr}}\left(e^{-\frac{L}{\lambda_s^{eff}}} - e^{-\frac{L+W_{cr}}{\lambda_s^{eff}}}\right) \\
R_{RE} = \frac{V_{RE}}{I_c} &= \frac{\overline{\mu_x}\gamma R_{sq}W_{gr}}{I_c} = \pm\frac{\gamma R_{sq}W_{gr}}{I_c}\frac{eP_iIR_{sq}{\lambda_s^{eff}}^2}{2W_{gr}W_{cr}}\left(e^{-\frac{L}{\lambda_s^{eff}}} - e^{-\frac{L+W_{cr}}{\lambda_s^{eff}}}\right) \\
&= \pm\frac{eP_i\gamma R_{sq}^2{\lambda_s^{eff}}^2}{2W_{cr}}\left(e^{-\frac{L}{\lambda_s^{eff}}} - e^{-\frac{L+W_{cr}}{\lambda_s^{eff}}}\right) \\
\Delta R_{RE} &= R_{RE}^{\rightarrow} - R_{RE}^{\leftarrow} = \frac{eP_i\gamma R_{sq}^2{\lambda_s^{eff}}^2}{W_{cr}}\left(e^{-\frac{L}{\lambda_s^{eff}}} - e^{-\frac{L+W_{cr}}{\lambda_s^{eff}}}\right) \qquad \text{(S3)}
\end{aligned}$$

We also want to quantify the Rashba-Edelstein effect using a dimensionless parameter. For this purpose, we assume that the spin currents are the source of the transverse charge currents and not the spin accumulations. For this, we use the formula derived inRef. 6.

$$\Delta R_{RE} = R_{RE}^{\rightarrow} - R_{RE}^{\leftarrow} = \frac{\alpha_{RE}P_iR_{sq}\lambda_s^{eff}}{W_{cr}}\left(e^{-\frac{L}{\lambda_s^{eff}}} - e^{-\frac{L+W_{cr}}{\lambda_s^{eff}}}\right) \qquad \text{(S4)}$$

Finally, to obtain an estimation for γ and α_{RE}, we assume that the entire observed signal arises from Rashba-Edelstein effect, i.e., $\Delta R_{SCC} = \Delta R_{RE}$. The extracted parameters from these operations are shown in the green rows of Table S1 for Sample A. For Sample B we did only see a clear signal for one of the configurations at 10 K.

S4.3. Quantification of the spin Hall effect in MoS_2

Because of the reduced spin lifetime of the MoS_2-covered graphene region it is not straightforward to determine the spin current which is absorbed by the semiconductor. However, we can estimate an upper limit of the signal expected if the spin current diffusing from the graphene channel into the MoS_2 is converted to a charge current due to the spin Hall effect in the MoS_2 channel.

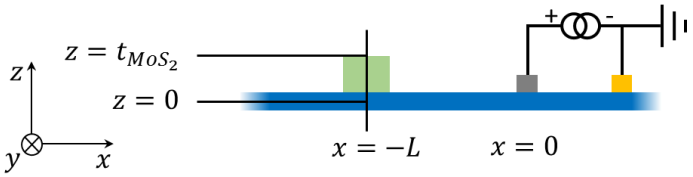

Figure S8. Sketch of the modeled geometry. The spin injector is grey, the Ti/Au contact is yellow, the graphene channel is blue, and the MoS_2 is green. The thickness of the graphene is assumed to be zero.

To evaluate the effect of spin absorption in a 1D approach which we can solve analytically, we assume that the width of the MoS_2 flake is significantly smaller than the spin relaxation length in the graphene channel ($W_{cr} \ll \lambda_s^{gr}$). We also ignore the role of the cross and assume that the graphene channel is 1D through all its length. With these assumptions, the modeled geometry is shown in Figure S8.

To model for this geometry, we break the device into different regions: I. The right side of the spin injector. II. From $x = 0$ to $x = -L$, III. MoS_2, from $z = 0$ to $z = t_{MoS_2}$, and IV. Graphene for $x < -L$. We write the spin accumulation in the different parts of the sample as follows:

$$\mu_I = Ae^{-\frac{x}{\lambda_s^{gr}}}$$
$$\mu_{II} = Be^{\frac{x}{\lambda_s^{gr}}} + Ce^{-\frac{x}{\lambda_s^{gr}}}$$
$$\mu_{III} = De^{\frac{z}{\lambda_s^{MoS_2}}} + Ee^{-\frac{z}{\lambda_s^{MoS_2}}}$$
$$\mu_{IV} = Fe^{\frac{x}{\lambda_s^{gr}}}$$

where $\lambda_s^{MoS_2}$ is the spin relaxation length at the MoS_2 and we have imposed that $\mu_s(x \to \pm\infty) \to 0$. To obtain the spin accumulation in the system we need to determine the coefficients $A - F$. For this purpose, we need 6 equations. We obtain three of them from imposing the continuity of μ_{IV} at $x = 0$ and $x = -L$.

To obtain the other 3 equations, we need to define the spin currents in the graphene and MoS_2 channels respectively:

$$I_s^{gr} = -\frac{W_{gr}}{eR_{sq}^{gr}}\frac{d\mu_s^{gr}}{dx}$$
$$I_s^{MoS_2} = -\frac{W_{gr}W_{cr}}{e\rho_{MoS_2}}\frac{d\mu_s^{MoS_2}}{dz}$$

Here, ρ_{MoS_2} is the resistivity of the MoS_2 channel, and W_{cr} is the width of the MoS_2 flake in Figure S8. By imposing the discontinuity of I_s^{gr} at $x = 0$, which is of $P_i I_c$ as discussed in section S2, the continuity of I_s^{gr} and $I_s^{MoS_2}$ at $x = L$, and $I_s^{MoS_2}(z = t_{MoS_2}) = 0$, that guarantees that there is no spin current leaving the MoS_2 flake, we obtain the remaining 3 equations.

From the derivation above, we obtain the spin currents and accumulations in the MoS_2 channel. However, we still need to convert them into voltages to determine the measured signal. A spin

current density in the MoS_2 channel ($J_s^{MoS_2} = \frac{I_s^{MoS_2}}{W_{gr}W_{cr}}$) induces a transverse charge current density $J_c^T = \frac{I_c^T}{W_{cr}t_{MoS_2}} = \theta_{SH}^{MoS_2}\frac{I_s^{MoS_2}}{W_{gr}W_{cr}}$ where $\theta_{SH}^{MoS_2}$ is the spin Hall angle of the MoS_2.

Because we are measuring the voltage in an open circuit configuration, we use: $V_{SH}^{MoS_2} = I_c^T R_{eff}$, where R_{eff} is the effective resistance of the MoS_2 and graphene. Because the resistance of the MoS_2 is considerably higher than that of the graphene channel, we need to take the effect of shunting by the graphene into account to determine R_{eff}. We assume that the system behaves like if the MoS_2 channel would be connected in parallel with the graphene:

$$R_{eff}^{-1} = R_{MoS_2}^{-1} + R_{gr}^{-1} = \frac{W_{cr}t_{MoS_2}}{W_{gr}\rho_{MoS_2}} + \frac{W_{cr}}{R_{sq}W_{gr}}$$

Finally,

$$V_{SH}^{MoS_2} = I_c^T R_{eff} = \theta_{SH}^{MoS_2}\frac{I_s^{MoS_2}t_{MoS_2}R_{eff}}{W_{gr}}$$

Because the spin current is not constant along the MoS_2 thickness we replace $I_s^{MoS_2}$ in the equation above by:

$$\bar{I}_s^{MoS_2} = \frac{1}{t_{MoS_2}}\int_0^{t_{MoS_2}} I_s^{MoS_2}(z)dz = \frac{W_{cr}W_{gr}}{et_{MoS_2}\rho_{MoS_2}}\left[D\left(1 - e^{t_{MoS_2}/\lambda_s^{MoS_2}}\right) + E\left(1 - e^{-t_{MoS_2}/\lambda_s^{MoS_2}}\right)\right]$$

Using the two equations above, we determine the voltage induced by the spin Hall effect in MoS_2, which we divide by the current applied to the spin injector to obtain the nonlocal resistance:

$$R_{SH}^{MoS_2} = \frac{V_{SH}^{MoS_2}}{I_C} = \theta_{SH}^{MoS_2}\frac{\bar{I}_s^{MoS_2}t_{MoS_2}R_{eff}}{I_cW_{gr}}$$

As explained above, the sign of $R_{SH}^{MoS_2}$ changes with the magnetization direction. Because our definition of the spin-to-charge conversion signal is $\Delta R_{SCC} = R_{SCC}^{\rightarrow} - R_{SCC}^{\leftarrow}$, we define $\Delta R_{SH}^{MoS_2} = 2R_{SH}^{MoS_2}$. The inputs of our model are $\lambda_s^{MoS_2}$,ρ_{MoS_2}, and $\theta_{SH}^{MoS_2}$ and are unknown to us, while the output is $\Delta R_{SH}^{MoS_2}$ and we know its value. To give an estimate for $\theta_{SH}^{MoS_2}$, we assume that $\lambda_s^{MoS_2} = 20$ nm, as estimated in Ref.7, we leave ρ_{MoS_2} as a free parameter and extract the $\theta_{SH}^{MoS_2}$ that gives a signal$\Delta R_{SH}^{MoS_2} = \Delta R_{SCC}$. The results from this model are shown in Figure S9 for sample A at 10 K. Because of the effect of shunting and the reduction of the spin currents which get absorbed by the MoS_2 as ρ_{MoS_2} increases, $R_{SH}^{MoS_2}$ presents a maximum value of 11.5 mΩ at $\rho_{MoS_2} = 7.1 \times 10^{-4}$ Ωm. This helps us to give an estimate of the best-case scenario for spin absorption that requires the lowest $\theta_{SH}^{MoS_2}$ to achieve the measured signal. We have adjusted $\theta_{SH}^{MoS_2}$ so that the maximum $R_{SH}^{MoS_2}$ corresponds to the measured signal. From this process we conclude that the minimal spin Hall angle required to achieve ΔR_{SCC} at 10 K in sample A is 3.3%. To estimate the temperature dependence of $\theta_{SH}^{MoS_2}$ for sample A, we have performed the same analysis described above assuming that the spin

relaxation length in MoS_2 does not depend on the temperature, which is the case if the Dyakonov-Perel mechanism is the dominant source of spin relaxation[8]. The results are shown in Table S1.

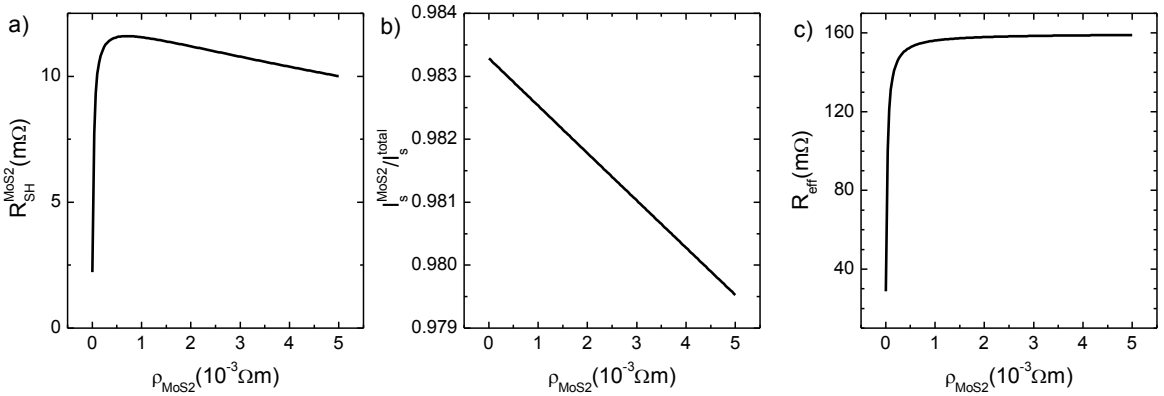

Figure S9. (a) Estimation of the spin signal induced by the spin Hall effect in the MoS_2 channel as a function of the MoS_2 resistivity using the parameters of Sample A at 10 K and by assuming $\theta_{SH}^{MoS_2} = 3.3$ %. (b) Ratio between the spin current diffusing into the MoS_2 ($I_s^{MoS_2}$) and spin current entering the graphene-MoS_2 junction in the model (I_s^{total}). The ratio decreases as ρ_{MoS_2} increases. (c) Effective resistance of the MoS_2 and graphene channel. Asρ_{MoS_2} increases, R_{eff} increases before saturating when the MoS_2 resistance becomes significantly higher than that of the graphene channel.

S5. Analysis of the measurements at different temperatures

S5.1. Sample A

Unlike the case of 10 K (Fig. 3a of the main text), we only have one magnetic injector configuration for the antisymmetric Hanle precession curves ($R_{NL}^{\uparrow}$) measured at 100 K, 200 K, and 300 K (Figure 4a of the main text). Hence, we cannot quantify the spin Hall angle in graphene for Sample A at these temperatures. In contrast, the μ_x-induced spin-to-charge conversion signals can be obtained from direct extrapolation of $R_{NL}^{\uparrow}$from high fields, as explained in section S3.1. The extracted signal ΔR_{SCC} is shown in Table S1.

S5.2. Sample B

For sample B, we have both magnetic configurations of the antisymmetric Hanle curves ($R_{NL}^{\uparrow}$ and $R_{NL}^{\downarrow}$) at 100, 200 and 300 K and, consequently, $\Delta R_{SH} = R_{NL}^{\uparrow} - R_{NL}^{\downarrow}$can be fit to Eq. S2. The extracted parameters are shown in Table S2. However, no clear μ_x-induced spin-to-charge conversion signal is observed at these temperatures. As an example, the measurements at 300 K are shown in Figure S10.

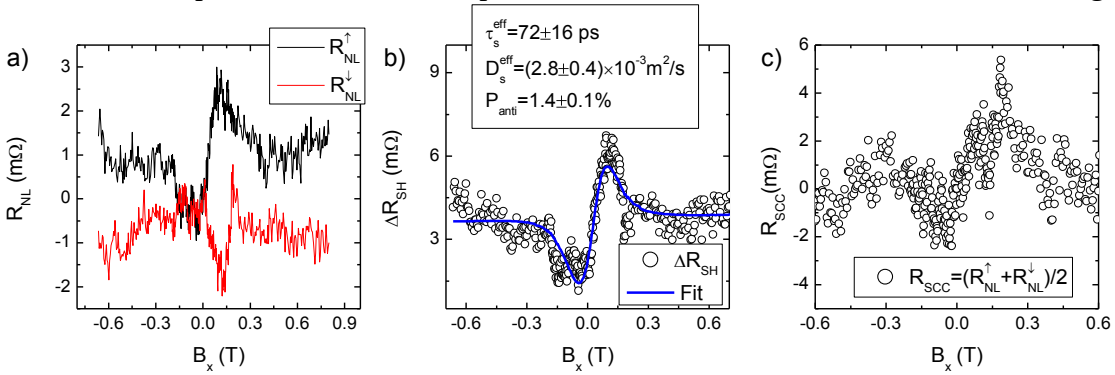

Figure S10. (a) Antisymmetric Hanle precession measurements for the two different orientations of the FM injector for sample B at 300 K. (b) ΔR_{SH} obtained as defined above by subtracting the components shown in (a) and its fit to Eq. S2 with the extracted parameters. (c) R_{SCC}. In this case ΔR_{SCC} is hard to extract because it is highly sensitive to the B field range selected for the extraction. However, it can be estimated to be between 3 and 5 mΩ.

S6. Extracted parameters for sample A and B

Table S1. Extracted parameters for sample A. D_s^{gr}, τ_s^{gr}, and P_{sym} are extracted from fits to the symmetric Hanle precession data, D_s^{eff}, τ_s^{eff}, and P_{anti} are extracted from fits to the antisymmetric Hanle precession data, and ΔR_{SCC} is extracted from fits to the S-shaped background of the antisymmetric Hanle precession data. γ and α_{RE} are obtained using ΔR_{SCC} and Eqs. S3-S4 with the spin transport parameters extracted from the antisymmetric Hanle precession data. The uncertainty ranges here are obtained considering only the uncertainty in ΔR_{SCC}.

Sample A	10 K	100 K	200 K	300 K
$R_{sq}^{gr}(\Omega)$	543	454	347	295
$R_{sq}^{TMD/gr}(\Omega)$	497	430	335	288
$D_s^{gr}(10^{-3}\mathrm{m}^2/\mathrm{s})$	5.7 ± 0.5	8.8 ± 0.5	8.8 ± 0.5	20 ± 4
τ_s^{gr} (ps)	300 ± 20	221 ± 8	221 ± 8	152 ± 6
$P_{sym}(\%)$	1.4 ± 0.1	1.35 ± 0.06	1.35 ± 0.06	2.3 ± 0.1
$P_{corr}(\%)$	2.9 ± 0.2	2.9 ± 0.1	2.9 ± 0.1	4.8 ± 0.2
$D_s^{eff}(10^{-3}\mathrm{m}^2/\mathrm{s})$	1.2 ± 0.1			
τ_s^{eff}(ps)	72 ± 7			
$P_{anti}(\%)$	3.6 ± 0.2			
$\theta_{SH}^{TMD/gr}(\%)$	4.5 ± 0.6			
$\sigma_{SH}^{Gr}(\Omega^{-1})$	$(9 \pm 1) \times 10^{-5}$			
$\Delta R_{SCC}(\mathrm{m}\Omega)$	11.5 ± 0.4	12 ± 0.5	6.7 ± 0.2	7.4 ± 0.5
$\gamma(\mathrm{A/(Jm)})$	$(2.9 \pm 0.1) \times 10^{20}$	$(1.63 \pm 0.07) \times 10^{21}$	$(3.02 \pm 0.09) \times 10^{21}$	$(3.3 \pm 0.2) \times 10^{21}$
$\alpha_{RE}(\%)$	0.85 ± 0.03	2.7 ± 0.1	3.32 ± 0.1	3.0 ± 0.2
$\theta_{SH}^{MoS_2}(\%)$	3.3 ± 0.1	4.1 ± 0.2	2.98 ± 0.09	2.2 ± 0.1

Table S2. Extracted parameters for sample B. The "Left" and "Right" labels refer to the data obtained with the spin injector placed at the left and right sides of the TMD-covered region, respectively.

Sample B	10 K	100 K	200 K	300 K
$R_{sq}^{gr}(\Omega)$				
$R_{sq}^{TMD/gr}(\Omega)$	282	266	231	215
$D_s^{gr}(10^{-3}\mathrm{m}^2/\mathrm{s})$	7.0 ± 0.3	11 ± 1	15 ± 2	16 ± 3
τ_s^{gr} (ps)	252 ± 8	146 ± 14	139 ± 2	114 ± 1
$P_{sym}(\%)$	2.4 ± 0.1	7.2 ± 0.1	7.7 ± 0.1	6.9 ± 0.1
$Right\ D_s^{eff}(10^{-3}\mathrm{m}^2/\mathrm{s})$	1.5 ± 0.1	1.6 ± 0.1	1.4 ± 0.1	2.8 ± 0.4
$Right\ \tau_s^{eff}$ (ps)	70 ± 9	49 ± 3	44 ± 3	72 ± 16
$Right\ P_{anti}(\%)$	3.4 ± 0.3	3.8 ± 0.3	3.1 ± 0.3	1.5 ± 0.1
$Right\ \theta_{SH}^{TMD/gr}(\%)$	4.8 ± 0.9	2.0 ± 0.5	1.2 ± 0.2	0.33 ± 0.04
$Right\sigma_{SH}(\Omega^{-1})$	$(17 \pm 3) \times 10^{-5}$	$(7.5 \pm 2) \times 10^{-5}$	$(5.2 \pm 0.9) \times 10^{-5}$	$(1.5 \pm 0.2) \times 10^{-5}$
$Left\ D_s^{eff}(10^{-3}\mathrm{m}^2/\mathrm{s})$	2.1 ± 0.1	1.5 ± 0.1		
$Left\ \tau_s^{eff}$ (ps)	73 ± 6	53 ± 2		
$Left\ P_{anti}(\%)$	1.9 ± 0.1	3.0 ± 0.2		
$Left\ \theta_{SH}^{TMD/gr}(\%)$	1.5 ± 0.2	1.3 ± 0.2		
$Left\ \sigma_{SH}^{Gr}(\Omega^{-1})$	$(5.3 \pm 7) \times 10^{-5}$	$(4.9 \pm 0.8) \times 10^{-5}$		

S7. Comparison between spin Hall effect in Pt and in TMD/graphene devices

S7.1. TMD/graphene normalized conversion efficiency

As shown in Section S2, the signal induced by the spin Hall effect in the case of TMD/graphene heterostructures is determined as:

$$\Delta R_{SH} = \frac{\Delta V_{SH}}{I_c} = 2\theta_{SH}^{TMD/gr} R_{sq}^{TMD/gr} \frac{\bar{I}_s}{I_c}$$

We want to determine an efficiency factor which is a trans-resistance defined as follows: $R_{eff}^{TMD/gr} = \Delta V_{SH}/I_s$ where I_s is the spin current entering the TMD/graphene heterostructure and $\Delta V_{SH} = \left(R_{NL}^{\uparrow} - R_{NL}^{\downarrow}\right) I_c$ is the transverse voltage output measured as shown in Figure S3. Since the measured signal depends on $\bar{I}_s$, the average spin current at the region where the conversion takes place, we rewrite the equation above in the following way:

$$\Delta V_{SH} = \left(\frac{2\theta_{SH}^{TMD/gr} R_{sq}^{TMD/gr} \bar{I}_s}{I_s} \right) I_s = R_{eff}^{TMD/gr} I_s$$

The efficiency factor is defined as follows:

$$R_{eff}^{TMD/gr} = \frac{2\theta_{SH}^{TMD/gr} R_{sq}^{TMD/gr} \bar{I}_s}{I_s}$$

To obtain $R_{eff}^{TMD/gr}$ we need to determine the correction factor $\bar{I}_s/I_s$, which can be done by considering that the spin current entering the TMD-covered graphene region is: $I_s(x) = (P_i I_c e^{-x/\lambda_s^{eff}})/2$ and the average spin current at the region of interest reads:

$$\bar{I}_s = \frac{1}{W_{cr}} \int_L^{L+W_{cr}} I_s(x) dx = \frac{P_i I_c}{2\, W_{cr}} \int_L^{L+W_{cr}} e^{-x/\lambda_s^{eff}} dx = \frac{P_i I_c \lambda_s^{eff}}{2\, W_{cr}} \left(e^{-L/\lambda_s^{eff}} - e^{-(L+W_{cr})/\lambda_s^{eff}} \right)$$

Now we can obtain the $\bar{I}_s/I_s$ factor:

$$\frac{\bar{I}_s}{I_s} = \frac{\lambda_s^{eff}}{W_{cr}} \frac{e^{-L/\lambda_s^{eff}} - e^{-(L+W_{cr})/\lambda_s^{eff}}}{e^{-L/\lambda_s^{eff}}} = \frac{\lambda_s^{eff}}{W_{cr}} \left(1 - e^{-W_{cr}/\lambda_s^{eff}} \right)$$

which for sample A at 10 K is 0.3. Now we finally write the efficiency factor for the TMD/graphene case:

$$R_{eff}^{TMD/gr} = \frac{2\theta_{SH}^{TMD/gr} R_{sq}^{TMD/gr} \lambda_s^{eff}}{W_{cr}} \left(1 - e^{-W_{cr}/\lambda_s^{eff}} \right)$$

This expression gives a numerical value of $R_{eff}^{TMD/gr} \approx 13.4\,\Omega$ for sample A at 10 K. Note that, because we have measured with magnetic fields applied in the x direction, there is still a correction factor required to account for the diffusive broadening of the spin precession, which we have estimated to be of about 0.62 using Eq. S2.

S7.2. Pt/graphene normalized conversion efficiency

We would like to compare the expression obtained above for $R_{eff}^{TMD/gr}$ with a properly normalized efficiency for Pt/graphene devices in which the spin Hall signal is determined by[9]:

$$\Delta R_{SH}^{Pt} = \frac{2\theta_{SH}^{Pt}\rho_{Pt}x_{Pt/gr}}{W_{Pt}}\frac{\bar{I}_s}{I_c}$$

Therefore, the efficiency factor can be obtained from this relation:

$$V_{SH}^{Pt} = \left(\frac{2\theta_{SH}^{Pt}\rho_{Pt}x_{Pt/gr}}{W_{Pt}}\frac{\bar{I}_s}{I_s}\right)I_s = R_{eff}^{Pt/gr}I_s$$

where, I_s is the spin current entering the Pt layer, θ_{SH}^{Pt} the spin Hall angle, ρ_{Pt} the resistivity, and W_{Pt} the width of the Pt wire.$x_{Pt/gr}$ is a parameter that accounts for the parallel conduction channel provided by the graphene that can reduce the measured voltage. In the case of graphene, however, because its sheet resistance is higher than Pt, $x_{Pt/gr} \approx 1$. The $\bar{I}_s/I_s$factor is [9, 10]:

$$\frac{\bar{I}_s}{I_s} = \frac{\lambda_{Pt}}{t_{Pt}}\frac{1-e^{-t_{Pt}/\lambda_{Pt}}}{1+e^{-t_{Pt}/\lambda_{Pt}}}$$

wheret_{Pt} is the thickness of the Pt wire and λ_{Pt} its spin diffusion length. Now we can write the efficiency for Pt as:

$$R_{eff}^{Pt/gr} = \frac{2\theta_{SH}^{Pt}\rho_{Pt}x_{Pt/gr}}{W_{Pt}}\frac{\lambda_{Pt}}{t_{Pt}}\frac{1-e^{-t_{Pt}/\lambda_{Pt}}}{1+e^{-t_{Pt}/\lambda_{Pt}}}$$

We estimate $R_{eff}^{Pt/gr} \approx 0.27\ \Omega$ using the following parameters from Ref. 9: $\theta_{SH}^{Pt} = 0.23$, $\rho_{Pt} = 134\ \mu\Omega$cm, $\lambda_{Pt} = 2$ nm, $W_{Pt} = 200$ nm, $t_{Pt} = 21$ nm.

The conversion efficiencies can now be directly compared by looking at the $R_{eff}^{Pt/gr}$ and $R_{eff}^{TMD/gr}$ values. Since $R_{eff}^{TMD/gr}$ is $\sim 50 \times R_{eff}^{Pt/gr}$, we conclude that the TMD-covered graphene is 50 times more efficient than highly resistive Pt for spin detection despite the fact that the spin Hall angle in Pt is an order of magnitude higher than in TMD-covered graphene. Note that, accounting for the spin precession used in our measurement leads to, $R_{eff}^{TMD/gr}/R_{eff}^{Pt/gr} = 31$, still a large difference.

S8. Theoretical calculation of spin-to-charge conversion in TMD/graphene heterostructures

To obtain a theoretical estimate to the magnitude of SHE and REE signals in our devices, we use a simplified model that captures the physics of a monolayer graphene/TMD heterostructure by using the following Hamiltonian[11-13]:

$$H = H_0 + H_I + H_R$$

where

$$H_0 = \hbar v_f\left(\sigma_x k_x + \tau_z\sigma_y k_y\right) + \Delta\sigma_z$$
$$H_I = (\lambda_I\sigma_z + \lambda_{VZ})\tau_z s_z$$

$$H_R = \lambda_R(s_y\sigma_x k_x - \tau_z s_x \sigma_y)$$

with σ_α, τ_α and s_α the Pauli matrices on the α direction acting on the pseudospin, valley and spin degrees of freedom, respectively. H_0 represents the orbital part, which is described by the Dirac's Hamiltonian with Fermi velocity v_f and a staggered potential with strength Δ, the latter appearing because of the broken sub-lattice symmetry of the TMD. H_I represents the intrinsic spin-orbit coupling of the heterostructure, modelled with a Kane-Mele term with strength λ_I and a valley-Zeeman coupling characterized by the parameter λ_{VZ}, both appearing because of the honeycomb structure and the broken sub-lattice symmetry. This term is responsible for the SHE, as we will show ahead. Finally, H_R represents the Rashba spin-orbit coupling arising from the interface between graphene and the TMD, with strength λ_R. This last term is the source of the REE. In this model we are excluding the so-called pseudospin inversion asymmetry terms[13], because they do not contribute to any of the effects of interest at low energy, and we use the tight-binding parameters from Ref. 13.

S8.1. The spin Hall effect

Despite the presence of the Rashba spin-orbit coupling, the origin of the spin Hall effect was traced back to the intrinsic spin-orbit coupling[11], described in these heterostructures by a valley-Zeeman and Kane-Mele spin-orbit coupling, which interacts with the staggered potential for producing a net berry phase and, therefore, a finite SHE. For simplicity, we can neglect the Rashba spin-orbit coupling, and consider the spin-up and spin-down bands as independent. Moreover, if we also neglect intervalley scattering, the Dirac's cone can also be considered as independent, leading then to 8 almost identical bands described by the dispersion relation

$$\varepsilon(\boldsymbol{k}, \tau, s) = s\lambda_{VZ} \pm \sqrt{\hbar(v_F k)^2 + {\Delta_{s,\tau}}^2},$$

where $\Delta_{s,\tau} = \Delta - \tau s \lambda_I$. Each of these bands will contribute the intrinsic spin Hall conductivity, and the calculation can be done following Refs. 14, 15, leading to the following result:

$$\sigma_{SH}(\varepsilon_F) = \frac{e^2}{2h}\sum_{s,\tau=\pm1}\tau\left[\Delta_{s,\tau}\frac{\Theta(|\Delta_{s,\tau}|-|\varepsilon_F-\tau s\lambda|)}{\sqrt{{\Delta_{s,\tau}}^2+(\varepsilon_F-\tau s\lambda)^2}} + \Theta(|\varepsilon_F-\tau s\lambda|-\Delta_{s,\tau})\right] \quad \text{(S5)}$$

where Θ is the Heaviside function. The comparison between this model and the curve simulated by solving numerically the Kubo formula for graphene/MoS_2 heterostructure is presented in Figure S11, where the small difference arises from the difference between the broadening functions used in the model (Lorentzian) and in the simulation (Lorentzian-like)[11]. Figure S12a shows the spin Hall conductivity over a range of Fermi energies for three different temperatures. At $T = 0$ one can see that the maximum of the spin Hall conductivity is achieved at two points at around $\pm$1eV, changing sign when crossing the charge neutrality point (CNP). Therefore, a negative spin Hall angle (as found in the main text) would be an indication of the Fermi level being at the valence band of graphene but close to the CNP. In addition, the spin Hall conductivity maximum is highly susceptible to temperature effects, where we see a linear variation with $\beta = 1/T$ at low and high temperature (Figure S12b). In this sense, the maximum spin Hall conductivity achieved in this system at low temperature is $0.2e^2/h$. This value is also suppressed by intervalley scattering[16], so it is difficult to establish an exact value, but assuming weak intervalley scattering and using the square resistance ($R_{sq}^{TMD/gr}$) extracted from sample A, one obtains a conversion efficiency in the range of $\theta_{SH}^{TMD/gr} = 1 - 10\%$, which is consistent with the experimental observation.

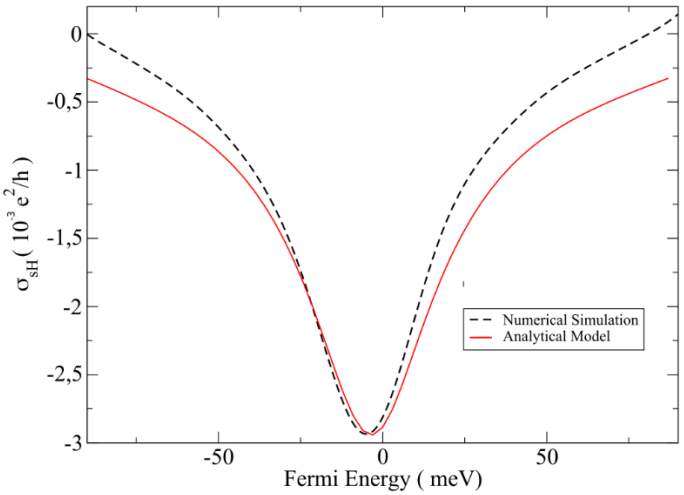

Figure S11. Comparison between the simulation of the spin Hall effect for graphene/MoS_2 heterostructure and the model based on individual spin bands. We have introduced a gaussian broadening of 20 meV to match the intrinsic broadening of the Kernel Polynomial Method (KPM) simulations performed at Ref. 11. The small difference is due to the broadening which is not energy independent in the KPM method.

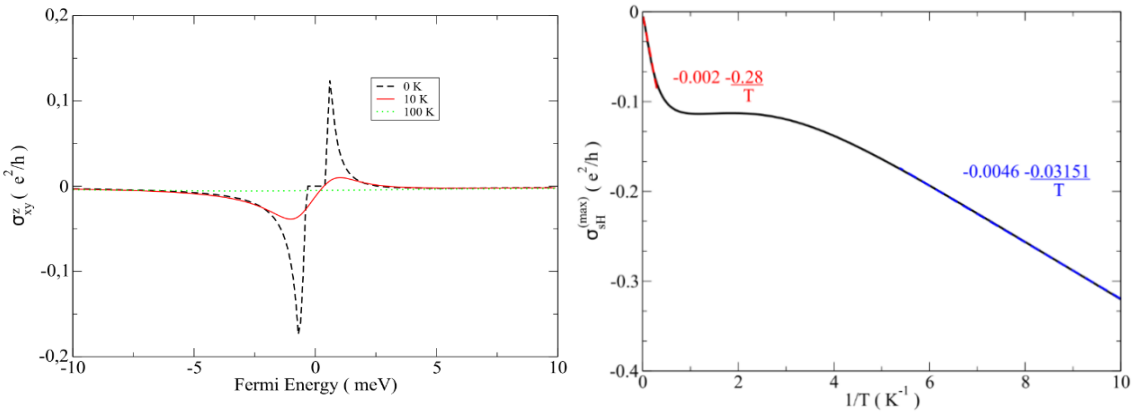

Figure S12. (a) Spin Hall conductivity as a function of Fermi energy for three different temperatures and (b) the evolution of the maximum of the spin Hall conductivity computed as a function of temperature, both computed using Eq. S5. Both results are obtained at zero gaussian broadening.

S8.2. The Rashba-Edelstein effect and its reciprocal

The REE is a phenomenon where the combined effect of a momentum dependent spin texture, and an external electric field $\boldsymbol{E}_0$ produces a nonequilibrium spin density $\boldsymbol{S}^{(neq)}$. It is usually described by the electrical spin susceptibility χ_{RE}, which under the linear response limit allow for writing the following constitute relation

$$\boldsymbol{S}^{(neq)} = \chi_{RE}(\boldsymbol{E}_0 \times \hat{k})\widehat{\boldsymbol{S}}^{(neq)}.$$

The polarization of the spin density is perpendicular to both the external electric field and the out-of-plane direction and is defined in units of a charge density. The REE is a dissipative effect and, as shown by Offidani et al.[17], for pure Rashba-like systems this implies that the spin susceptibility is proportional to the DC conductivity (σ_{DC})

$$\frac{\chi_{RE}}{\sigma_{DC}} = \frac{1}{v_{RE}},$$

where v_{RE} is a parameter with units of velocity characterizing the spin-to-charge conversion efficiency. There are different calculations of this parameter. We have, for instance, the phenomenological result of Dyrdal[14] :

$$\frac{v_F}{v_{RE}} = \frac{1}{2}\frac{2+x}{1+x}\Theta(2-x) + \frac{x}{x^2-1}\Theta(x-2), \text{ with } x \equiv \varepsilon_F/\lambda_R,$$

the self-consistent and fully microscopic calculation performed by Offidani et al.[17] which corrects the energy dependences to:

$$\frac{2v_F}{v_{RE}} = \Theta(2-x) + 2xg(D_c)\Theta(x-2), \text{ with } x \equiv \varepsilon_F/\lambda_R,$$

where $g(D_c)$ is a dimensionless parameter that depends of the disorder, and the result of Garcia et al.[11], which takes into account all the spin-orbit parameters leading to a higher spin density for high energies but to a small $1/v_{RE}$ due to the broadening effects present in the system, which will increase σ_{DC}close to the CNP.

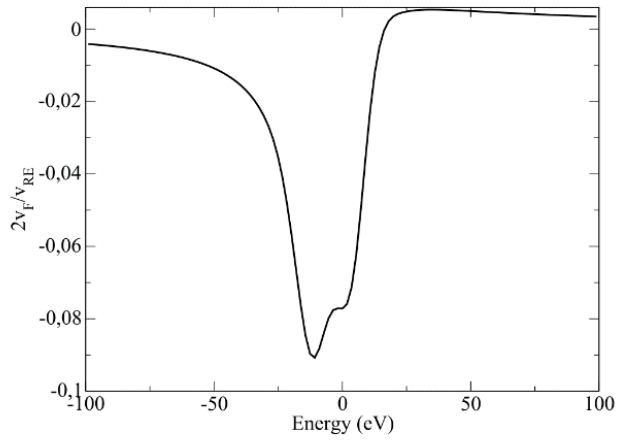

Figure S14. Figure of merit $2v_F/v_{RE}$of the Rashba Edelstein effect for graphene/MoS_2 heterostructure considering a broadening of 5 meV.

Using $2v_F/v_{RE}$ as a figure of merit, it is possible to extract a conversion efficiencyα_{RE} by computing the transformation from spin density to spin current using Fick's law[1]:

$$\alpha_{RE} = \frac{J_s^y}{J_x} = \frac{D_s}{\lambda_s v_{RE}}$$

where D_s and λ_s are the spin diffusion constant and the spin relaxation length of graphene. One should keep in mind that in this process there is no electric field affecting the spin current; therefore, the charge current density is obtained solely from the spin density. Using D_s and λ_s obtained from sample A, one obtains a conversion efficiency α_{RE} ~0.1% in the best-case scenario, decreasing down to ~0.01% at higher temperatures. One should also keep in mind that there is an additional suppression term which appears due to the averaging over the channel width, which will further suppress this value.

The REE conversion efficiency α_{RE}changes sign following the same trend as the spin Hall angle $\theta_{SH}^{TMD/gr}$, because both effects originate from the proximity-induced spin-orbit coupling of graphene. Therefore, both α_{RE} and $\theta_{SH}^{TMD/gr}$have the same sign. This is not observed in our experiment, ruling out the REE as the origin of the in-plane spin-to-charge conversion signal.

S9. Scanning electron and atomic force microscopy imaging of sample A

After the electrical characterization we imaged our device with scanning electron microscopy (SEM), see Figure S15. We extracted the length and width of the graphene channels as well as the width of the ferromagnetic electrodes and their distances from these measurements. As the samples were in contact with air after the electrical characterization in vacuum, the Co electrodes are oxidized in the images.

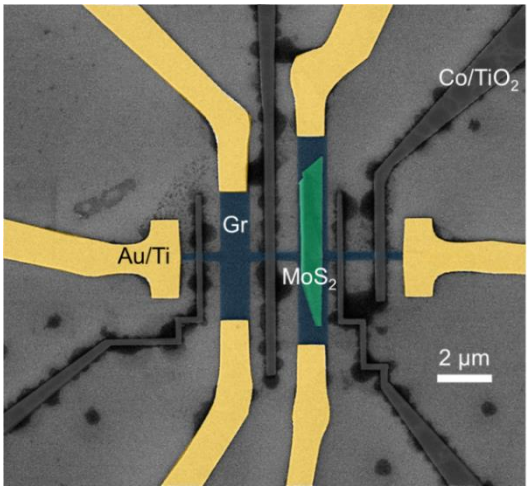

Figure S15. False-colored scanning electron microscopy image of Sample A. The width of the horizontal graphene (in blue) channel is 350 nm. The width of the MoS_2 flake (in green) and the two vertical graphene channels are 0.9 µm and 1.2 µm respectively.

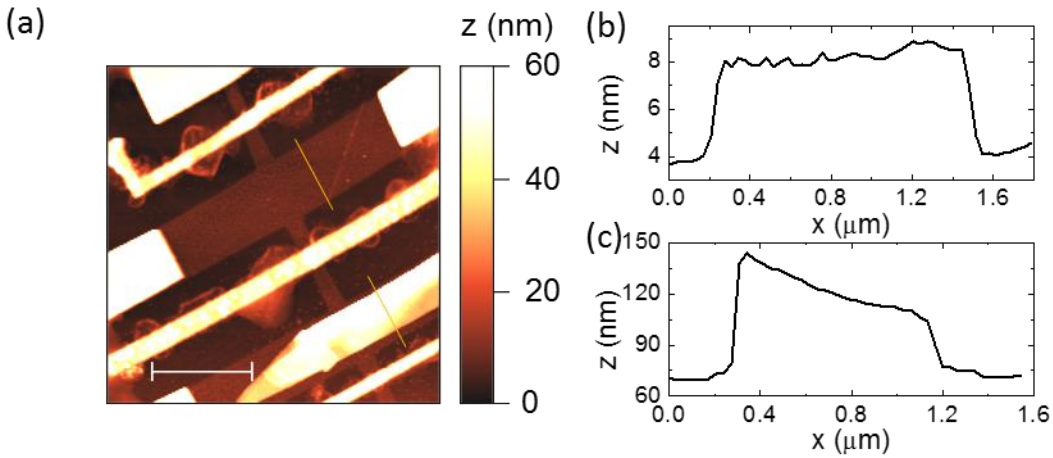

Figure S16. Atomic force microscopy characterization of Sample A. (a) Area scan showing the topography of the device. The scale bar is 2 µm long. (b) Line profile taken along the marked line in (a) across the graphene flake, where the thickness of the graphene flake is extracted to be roughly 5 nm, equivalent to around ten layers[19]. (c) Line profile taken along the marked line in (a) across the MoS_2 flake, where the thickness of the MoS_2 flake is between 35 and 75 nm.

After the electrical characterization and SEM imaging we measured the topography of device with an atomic force microscope (Agilent 5500) in tapping mode (Figure S16). The main result of this measurement is the height profile of the graphene/MoS_2 stack, as we extracted all lateral distances from the SEM image. The thickness of the graphene flake was determined to be roughly 5 nm. The MoS_2 flake shows a ramp-like shape on top and is between 35 and 75 nm thick.

References

1. Fabian, J.; Matos-Abiaguea, A.; Ertlera, C.; Stano, P.; Zutic, I. Semiconductor spintronics. *Acta Physica Slovaca*. **2007**, 57, 565–907.
2. Maassen, T.; Vera-Marun, I. J.; Guimarães, M. H. D.; van Wees, B. J. Contact-induced spin relaxation in Hanle spin precession measurements. *Phys. Rev. B.* **2012**, 86, 235408.
3. Stoner, E. C.; Wohlfarth, E. P. A mechanism of magnetic hysteresis in heterogeneous alloys. *Philos. Trans. Royal Soc. A.* **1948**, 240, 599–642.
4. Huertas Hernando, D.; Nazarov, Y. V.; Brataas, A.; Bauer, G. E. W. Conductance modulation by spin precession in noncollinear ferromagnet normal-metal ferromagnet systems. *Phys. Rev. B.* **2000**, 62, 5700–5712.
5. Crooker, S. A.; Furis, M.; Lou, X.; Adelmann, C.; Smith, D. L.; Palmstrøm, C. J.; Crowell, P. A. Imaging spin transport in lateral ferromagnet/semiconductor structures. *Science*. **2005**, 309, 2191–2195.
6. Zhang, S. Probing spin currents in semiconductors. *J. Appl. Phys*. **2001**, 89, 7564–7566.
7. Yan, W.; Txoperena, O.; Llopis, R.; Dery, H.; Hueso, L. E.; Casanova, F. A two-dimensional spin field-effect switch. *Nat. Commun*. **2016**, 7, 13372.
8. Schmidt, H.; Yudhistira, I.; Chu, L.; Neto, A. H. C.; Özyilmaz, B.; Adam, S.; Eda, G. Quantum transport and observation of Dyakonov-Perel spin-orbit scattering in monolayer MoS_2. *Phys. Rev. Lett.* **2016**, 116, 046803.
9. Yan, W.; Sagasta, E.; Ribeiro, M.; Niimi, Y.; Hueso, L. E.; Casanova, F. Large room temperature spin-to-charge conversion signals in a few-layer graphene/Pt lateral heterostructure. *Nat. Commun*. **2017**, 8, 661.
10. Torres, S. W.; Sierra, J. F.; Benítez, L. A.; Bonell, F.; Costache, M. V.; Valenzuela, S. O. Spin precession and spin Hall effect in monolayer graphene/Pt nanostructures. *2D Mater*. **2017**, 4, 041008.
11. Garcia, J. H.; Vila, M.; Cummings, A. W.; Roche, S. Spin transport in graphene/transition metal dichalcogenide heterostructures. *Chem. Soc. Rev*., **2018**, 47, 3359–3379.
12. Gmitra, M.; Kochan, D.; Högl, P.; Fabian, J. Trivial and inverted Dirac bands and the emergence of quantum spin Hall states in graphene on transition-metal dichalcogenides. *Phys. Rev*. B. **2016**, 93, 155104.
13. Cysne, T. P.; Ferreira, A.; Rappoport, T. G. Crystal-field effects in graphene with interface-induced spin-orbit coupling. *Phys. Rev. B.* **2018**, 98, 045407.
14. Dyrdał, A.; Dugaev, V. K.; Barnaś, J. Spin Hall effect in a system of Dirac fermions in the honeycomb lattice with intrinsic and Rashba spin-orbit interaction. *Phys. Rev*. B. **2009**, 80, 155444.
15. Sinitsyn, N. A.; Hill, J. E.; Min, H.; Sinova, J.; MacDonald, A. H. Charge and spin Hall conductivity in metallic graphene. *Phys. Rev. Lett*. **2006**, 97, 106804.
16. Garcia, J. H.; Cummings, A. W.; Roche, S. Spin Hall effect and weak antilocalization in graphene/transition metal dichalcogenide heterostructures. *Nano Lett*. **2017**, 17, 5078–5083.
17. Offidani, M.; Milletarì, M.; Raimondi, R.; Ferreira, A. Optimal Charge-to-Spin Conversion in Graphene on Transition-Metal Dichalcogenides. *Phys. Rev. Lett*. **2017**, 119, 196801.
18. Koh, Y. K.; Bae, M. H.; Cahill, D. G.; Pop, E. Reliably Counting Atomic Planes of Few-Layer Graphene (n > 4). *ACS Nano*. **2011**, 5, 269–274.